Lecture 6: Water and Radiation in the Climate System

Kerry Emanuel; notes by Joe Fitzgerald and Jörn Callies

June 23

1 Introduction

Over the next two lectures we will progress toward problems involving the interaction of water substances and radiation that lie at the frontier of climate research. At the end of the previous lecture, we left off with a discussion of moist radiative-convective equilibrium (RCE). Using a single column model with many levels in the vertical, we solved the band-integrated radiative transfer equations coupled to a representation of moist convection and obtained a temperature profile $T(z)$ that was an essentially realistic representation of the temperature profile of the tropical atmosphere. We note, however, that obtaining a realistic temperature profile is not a stringent test of our model's moist convection scheme: the observed $T(z)$ profile is relatively easily reproduced, because it follows the moist adiabat in the bulk of the troposphere.

Moist RCE is a good starting point for our understanding of the tropical atmosphere's leading-order structure, and examining our RCE solution can lead us to several physically important observations. By comparing the temperature profile resulting from RCE to that which results from radiative equilibrium, we see that the troposphere is cooling radiatively. Additionally, the RCE temperature profile indicates that the temperature at the tropical tropopause is approximately $-80°C$, a value which may remain fixed even as the climate changes. However, our RCE model also failed to reproduce some features of the real atmosphere, especially those due to the large-scale circulation, which was only crudely represented by an increased albedo. In the tropical upper troposphere/lower stratosphere, the observed temperature profile is shifted somewhat upward compared with our RCE calculation. This is due to the Brewer-Dobson circulation, a meridional overturning circulation in the tropical stratosphere which features upwelling through the tropical tropopause. This circulation can produce temperature deviations near the tropopause relative to our RCE solution because the timescale of radiation is not fast compared with that of the Brewer-Dobson upwelling.

2 The Earth's Energy Balance from Observations

We now move on to a reckoning of the Earth's energy balance based on observations. To build intuition, we consider what happens to solar energy as it arrives at Earth. Although the real atmosphere is continuous in the vertical, for simplicity we consider the energy balance by separating the atmosphere's vertical structure into three boxes: the troposphere,

the stratosphere, and the surface (which we take to include land as well as ocean). As a normalization, we consider the passage of 100 units of solar radiation (which could be thought of as individual photons) through the atmosphere. Figure 1 shows a schematic of how this solar radiation is passed between our three boxes.
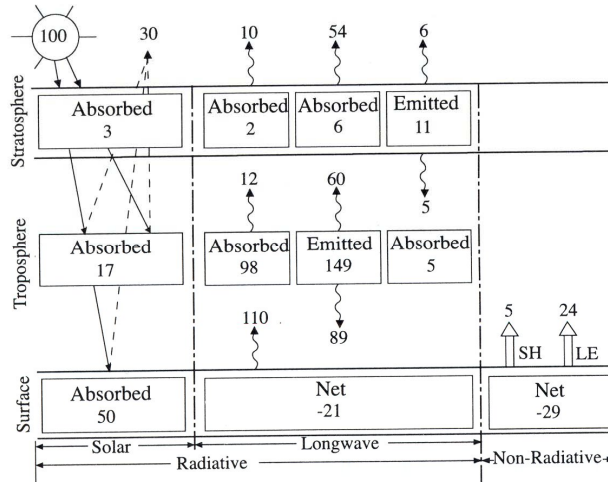
Figure 1: A schematic of the Earth's energy balance. The atmosphere is separated into surface, troposphere, and stratosphere boxes, and we consider the passage of 100 units of solar radiation through the system. The values in each box indicate how much energy is passed from box to box by various transfer processes.

In this approximate picture of the energy balance, 30 units of shortwave (SW) radiation are reflected back to space. The largest fraction of this reflection is due to clouds, and the next largest fraction is due to ice on the surface. After reflection, 70 units remain to be absorbed by the atmosphere and surface. Three of these units are absorbed in the stratosphere. This absorption filters harmful incoming UV photons out of the incoming SW radiation field. The troposphere absorbs 17 of the remaining units, with water vapor and clouds being the dominant absorbers. The 50 remaining units of SW are absorbed by the surface. These SW contributions to the energy balance are indicated on the left-hand side of Fig. 1.

The longwave (LW) contributions to the energy balance are shown in the centre portion of Fig. 1. The surface emits 110 units of LW radiation toward space. Eighty-nine of these units are absorbed and re-emitted back toward the surface by the troposphere. Note that this downwelling LW flux is greater than the 50 units the surface receives directly from the sun. The troposphere also emits 60 units upward toward space. The asymmetry between the 89 units of downward emission and 60 units of upward emission results from our bulk averaging over the troposphere and from the variations of temperature with height.

As discussed in previous lectures, the lower atmosphere is in thermodynamic disequilibrium with the surface. This thermal discontinuity drives a turbulent flux of enthalpy from the surface to the atmosphere with both sensible and latent heat components. These non-radiative surface fluxes are indicated on the right-hand side of Fig. 1.

The net contributions to the energy budget from solar SW radiation, LW radiation, and

the non-radiative surface fluxes are shown at the bottom of Fig. 1. Note that these values indicate that the primary cooling mechanism in the tropics is not radiation: the net effect of outgoing LW radiation in the tropics is small when the 89 units of longwave returning to the surface from the atmosphere are taken into account. The main balance in the tropics is instead between incoming solar radiation and evaporation. This implies that the tropical surface is much cooler than it would otherwise be if water could not evaporate, assuming that water vapor was still present in the atmosphere.

3   Contributions of Various Absorbers to the Temperature Profile

We now consider the effects of various greenhouse gases (GHGs) on the tropical temperature profile. As a simple conceptual method to assess the effect of each gas, we re-run the RCE column model (which includes variable clouds interacting with radiation) with GHGs removed one at a time from the column and compare the resulting temperature profile with our original RCE solution. The result of this procedure is shown in Fig. 2.
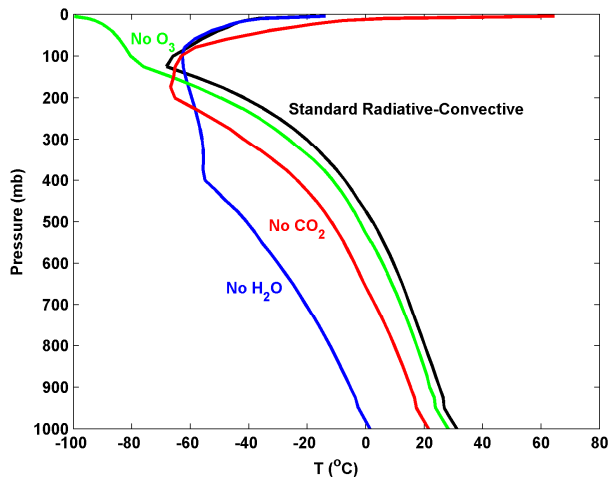
Figure 2: Temperature profiles $T(z)$ in RCE computed using a single-column model. Greenhouse gases are removed one at a time from the model and the equilibrium profile is computed to demonstate the approximate effect that each gas has on $T(z)$.

In the absence of CO_2 (red curve), the tropospheric temperature profile remains on a moist adiabat but is approximately $10°C$ colder than the original RCE profile. The stratospheric temperature, on the other hand, increases substantially. This stratospheric warming occurs because O_3 continues to absorb UV radiation but CO_2 is no longer available to emit infrared (IR) radiation toward space. The stratospheric thus warms to radiate additional energy and retain energy balance.

Removal of O_3 from the column model (green curve) also reduces the tropospheric temperature slightly, as O_3 has a weak greenhouse effect in the troposphere. In the stratosphere, removing O_3 results in a significant cooling as absorption of incoming UV no longer occurs.

Removal of water vapor from the column model (blue curve) results in a much colder troposphere alongside significant changes in the vertical structure of $T(z)$ in the upper troposphere. Some of the change in vertical structure may be artificial, as water vapor interacts chemically with other GHGs and we do not include these effects in our model.

The stratosphere is compressed into the uppermost portion of Fig. 2 due to the use of pressure coordinates. To show the effects of various gases on the stratospheric temperature more clearly, we plot the RCE profiles again in Fig. 3 using log-pressure coordinates. Comparison of the profiles computed in the absence of O_3 (green curve) and CO_2 (red curve) with the standard RCE profile (black curve) demonstrates that O_3 and CO_2 have strong and opposite-sign effects on stratospheric temperatures. As the first order radiative balance of the stratosphere is between UV absorption by ozone and IR emission by CO_2, removal of ozone cools the stratosphere while removal of CO_2 warms the stratosphere. The RCE calculation without O_3 also indicates that UV absorption in the stratosphere is not required to produce a tropopause: a transition in the shape of the temperature profile from moist adiabatic to a stable profile in radiative balance still occurs near the same level as in the standard RCE solution, although this transition is less sharp when O_3 is absent.
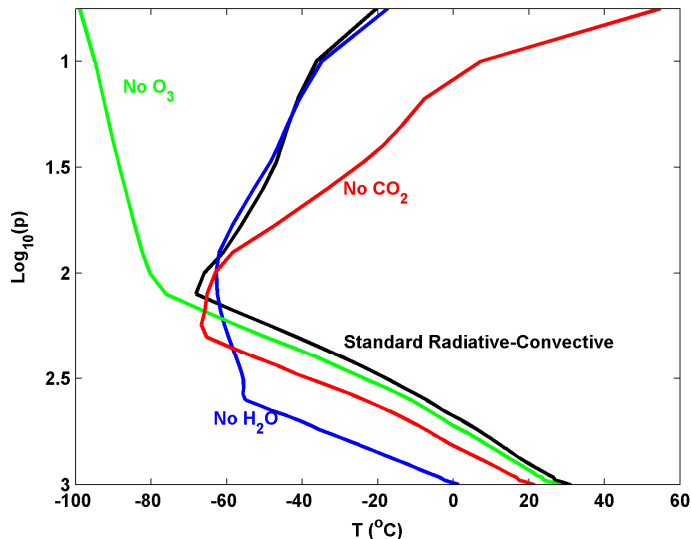
Figure 3: As in Fig. 2, but with log-pressure on the vertical axis to show the stratosphere more clearly.

4 Timescale of Approach to Radiative-Convective Equilibrium

4.1 Observations from a Single-Column Model

We now turn our attention to a basic physical issue: If $T(z)$ is perturbed away from its RCE solution, on what timescale does $T(z)$ return to the RCE state? Figure 4 shows the first ten days of the approach to equilibrium in our RCE column model. The time-

dependent calculations assume a fixed relative humidity profile, taken from the original RCE solution. The initial condition is an isothermal atmosphere, indicated by the Day 0 curve in Fig. 4. After ten days, $T(z)$ is still changing significantly with time. Further time evolution is shown in Fig. 5, which shows $T(z)$ in 15-day increments beginning from the state of the atmosphere at Day 10. After 25 days the tropospheric temperature has essentially returned to its RCE state, but the stratosphere takes much longer to return to equilibrium. Temperature variations in the stratosphere do not become small until nearly Day 150. Note that this long stratospheric return timescale is comparable to the change of the seasons, which implies that there is a lag in the stratospheric response to the seasonal cycle. As we will discuss later in this lecture, the coupling between the atmosphere and the surface (taken to be an ocean surface in these calculations; on land one would have to specify the water availability) is critical to these results. We also note that, in the stratosphere, $T(z)$ features small-scale vertical structures that persist for a long time during the return to equilibrium. These are likely due to small-scale structure in the specified relative humidity profile and the long timescale associated with water vapor in the stratosphere.
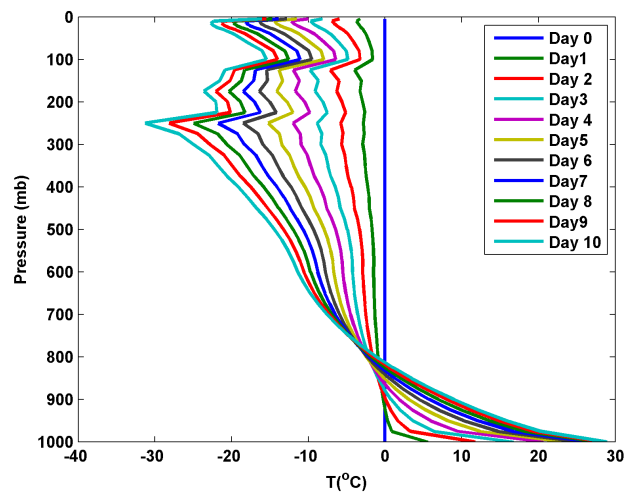
Figure 4: Daily snapshots of the temperature profile from a single-column model during evolution toward RCE. The initial condition is an isothermal atmosphere, and relative humidity is specified based on the RCE state.

4.2 A Simple Model of Relaxation to RCE

To better understand the controls on the timescale of the atmosphere's return to RCE, we now examine a simple analytical model recently presented in Cronin, T.W. and K. A. Emanuel, 2013: The climate time scale in the approach to radiative-convective equilibrium. *J. Adv. Model. Earth Sys.*, **5**, doi:10.1002/jame.20049. The goal is to strip this problem down to its essence. As we will see, this model reveals an important counter-intuitive result.
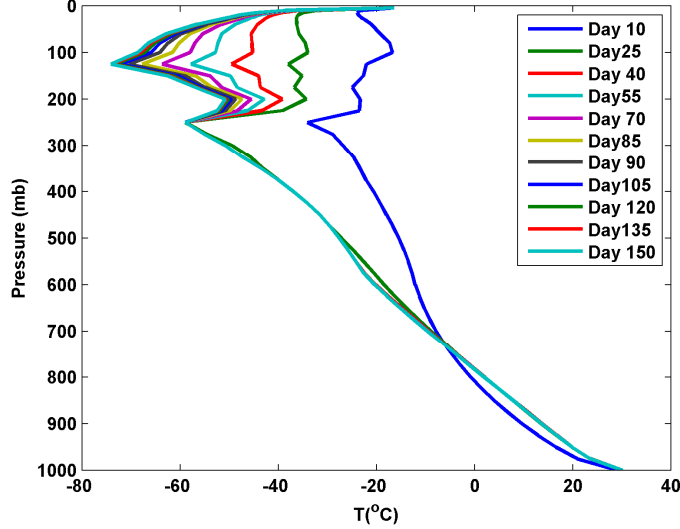
Figure 5: As in Fig. 4, but with snapshots every 15 days to show the slow evolution of the stratosphere toward equilibrium.

4.2.1 Temperature and Moist Static Energy Profiles in the Analytical Model

Figure 6 shows a schematic of our model setup. We consider an atmospheric column coupled to an ocean surface with mixed layer depth Δz_{ML}. The temperature profile is assumed to lie on a moist adiabat between the top of the boundary layer and the tropopause. This is equivalent to the statement that the saturation moist static energy (MSE) is constant with height up to the tropopause, where

$$h = c_p T + L_v q + gz \tag{1}$$

is the MSE and

$$h^\star = c_p T + L_v q^\star + gz \tag{2}$$

is the saturation MSE. Here c_p is the heat capacity of air at constant pressure, T is the temperature, L_v is the latent heat of vaporization of water, q is the specific humidity, $q^\star$ is the saturation specific humidity, g is the gravitational acceleration, and z is the height. MSE and saturation MSE are useful quantities as they are conserved during adiabatic and saturated adiabatic motions of air parcels, respectively.

To understand the equivalence of the two conditions 1) that the temperature profile lies on a moist adiabat (i.e., the column is neutral to moist convection) and 2) that the saturation MSE is constant with height, we consider the following argument. Suppose we adiabatically lift a parcel from some level z_1 to a higher level z_2. The parcel initially has the saturation MSE of the environmental profile at z_1, so that $h^\star_{\mathrm{parcel}} = h^\star(z_1)$. The parcel retains this value of saturation MSE during its adiabatic ascent and arrives at level z_2 with $h^\star_{\mathrm{parcel}} = h^\star(z_1)$. The environmental air at z_2 has saturation MSE $h^\star_{\mathrm{environment}} = h^\star(z_2)$. The difference between the saturation MSE of the parcel and that of the environment is then given by

$$h^\star_{\mathrm{parcel}} - h^\star_{\mathrm{environment}} = c_p(T_{\mathrm{parcel}} - T_{\mathrm{environment}}) + L_v(q^\star_{\mathrm{parcel}} - q^\star_{\mathrm{environment}}) \tag{3}$$

64

or equivalently,

$$h^\star(z_1) - h^\star(z_2) = c_p(T_{\text{parcel}} - T(z_2)) + L_v(q^\star_{\text{parcel}} - q^\star(z_2)). \tag{4}$$

No contribution to this saturation MSE difference arises from the gz term as we compare the parcel to the environment at the same altitude. To assess stability we are interested in the sign of the temperature difference appearing on the RHS of this equation: if $T_{\text{parcel}} > T_{\text{environment}}$, our lifted parcel will continue to rise and the column is unstable. The sign of this temperature difference can be inferred directly from the sign of the saturation MSE difference because the saturation specific humidity $q^\star$ is an increasing function of temperature at a given pressure. That is, if $T_{\text{parcel}} > T_{\text{environment}}$, then $q^\star_{\text{parcel}} > q^\star_{\text{environment}}$. This means that the two terms on the RHS must have the same sign. So, if the LHS is positive, both terms on the RHS must be positive, and similarly if the LHS is negative. The condition for convective neutrality is then that the saturation MSE is constant with height and equal to the actual MSE of the subcloud layer, so that both terms on the RHS are zero and adiabatically lifted parcels are neutrally buoyant.

As discussed in previous lectures, the ocean surface is in thermodynamic disequilibrium with the lower atmosphere. This thermodynamic disequilibrium is primarily due to a jump in moisture properties: the temperature at the bottom of the atmospheric boundary layer is close to that of the sea surface. However, boundary layer air is unsaturated, with a jump to saturation occurring very close to the sea surface. This leads to a discontinuity in h at the surface. (Note, however, that $h^\star$, whose profile is not shown in the boundary layer in Fig. 6, is nearly continuous at the surface due to the near agreement of atmospheric and surface temperatures.) As the boundary layer air is unsaturated, water vapor does not condense until parcels are lifted sufficiently high. The level at which condensation first occurs is referred to as the lifted condensation level, and below this level, the temperature profile assumes the dry adiabatic lapse rate. The MSE is constant with height in this dry adiabatic region: $c_p T + gz$ is constant with height due to the adiabatic lapse rate and q is constant with height due to homogenization of q in the vertical by dry convective turbulence. (In reality, q is only approximately constant with height and actually exhibits a slight decrease as we move up through the boundary layer. MSE therefore decreases in correspondence with the q variations.) Above the dry adiabatic region, the atmospheric temperature profile follows a moist adiabat up the the tropopause. Above the tropopause, radiative equilibrium leads to an increase in h with height, indicating stability to convection.

The "sickle" shape of the MSE profile $h(z)$ in Fig. 6 also warrants explanation. As mentioned above, h is constant in the boundary layer as water does not change phase and q is approximately constant with height. Between the top of the boundary layer and the tropopause, $h(z)$ exhibits a minimum as a function of height, even though h is conserved under adiabatic displacements. To understand the shape of $h(z)$, we note that moist convection occurs in a small fractional area of the atmosphere, and that in the remainder of the atmosphere we have large-scale subsidence balanced by radiative cooling. This radiative cooling acts to decrease the MSE of the descending air, causing h to decrease as we move down through the column starting from the tropopause. As we continue to descend, the $h(z)$ profile begins to increase again before we reach the dry adiabatic region in which h is constant. This increase of MSE is due to the action of shallow convection which mixes high-MSE boundary layer air into the lower levels of the free troposphere.

65
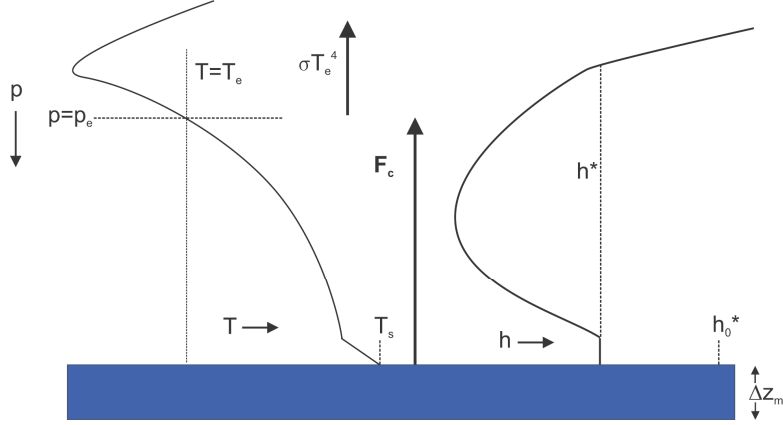
Figure 6: Schematic temperature $T(z)$, moist static energy $h(z)$, and saturation moist static energy $h^\star(z)$ profiles for our analytical model.

4.2.2 The Effect of Greenhouse Gases in the Analytical Model

Greenhouse gases are represented in the analytical model through their effect on the pressure level p_e at which the temperature on the moist adiabat equals the emission temperature $T_e = 255$ K. The effect of changing GHG concentrations in this model is shown schematically in Fig. 7. Increasing GHG concentrations causes the emission level to move upward (p_e to decrease). The moist adiabat that the tropospheric temperature profile follows is determined by the emission level p_e and the emission temperature T_e. Increasing the emission level then shifts the temperature profile onto a warmer moist adiabat. Alternatively, we can think of the moist adiabat as being determined by its value of saturation MSE, which in turn depends on T_e and p_e: $h^\star = h^\star(T_e, p_e)$.

Comparison of the adiabatic temperature profiles before and after the addition of GHGs in Fig. 7 demonstrates that temperature change at the original emission level ΔT_a is larger than the temperature change ΔT_s at the surface. Differential warming with height is a result of the curvature of the moist adiabat. For parameter values appropriate for today's atmosphere, this effect implies that a temperature increase of $3°$ at the emission level maps to a temperature increase of only $1°$ at the surface. This points to two competing climate feedbacks associated with water vapor: 1) The positive water vapor feedback due to increasing water vapor concentrations in warmer climates. 2) The ratio of surface warming to emission level warming decreases as the climate warms due to changes in the curvature of the moist adiabat. This second effect, known as the lapse rate feedback, can be thought of as buffering of surface temperature changes by evaporation.

It is important to note, however, that it is the wet bulb temperature, rather than the absolute temperature, that is most important to human comfort. The wet bulb temperature is defined as the temperature that an air parcel would have if it were cooled to saturation. This distinction is important, since even though future surface warming will be buffered by water vapor, humans will still feel the increased surface humidity. The biological upper bound is $35°$C wet bulb temperature, past which human beings cannot survive. In the present climate, a maximum of $33°$C is reached in the tropics, so it is likely that the

66

biological limit will be exceeded in global warming. Air conditioning can alleviate that, but will also likely increase GHG emissions even more.

The diurnal cycle of incoming solar radiation has important effects on tropospheric temperature which we exclude here by taking a single average value for the incoming solar radiation. In making such an approximation we introduce an error, as the average temperature resulting from the real diurnal cycle is not equal to the temperature that would result from constant insolation at the diurnal average value. This rectification of the diurnal cycle arises from the nonlinear dependence of the surface enthalpy fluxes on the surface temperature disequilibrium as well as from additional effects due to the radiative effects of clouds.
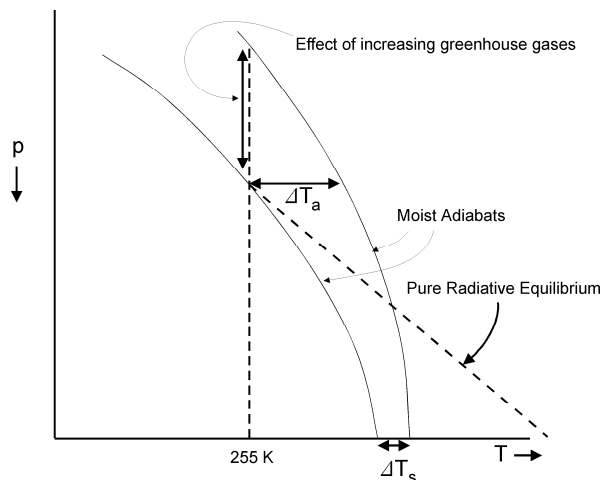
Figure 7: Schematic demonstrating the effect of adding greenhouse gases in our analytical model. The addition of GHGs moves the emission level upward and shifts the temperature onto a warmer moist adiabat.

4.2.3 Energy Balance in the Analytical Model

We now formulate the energy balance equations for our analytical model and study their linear stability to determine the timescale of relaxation to RCE. Based on the approximate surface energy balance inferred from observations in Section 2, we assume that the net LW flux at the surface is zero, and that that the steady-state energy balance in the troposphere is between the bulk turbulent flux of enthalpy F_c through the boundary layer (primarily due to evaporation) and IR emission to space σT_e^4 (see Fig. 6):

$$F_c = \rho_s C_k |V_s|(h_0^\star - h^\star) = \sigma T_e^4. \tag{5}$$

Here ρ_s is the density of air near the surface, C_k is the enthalpy exchange coefficient, V_s is the surface velocity provided by large-scale dynamics, σ is the Stefan-Boltzmann constant, $h^\star$ is the vertically-constant value of saturation MSE in the free troposphere and T_e is the emission temperature corresponding to the solar forcing. Equation (5) allows us to write the saturation MSE of the ocean surface $h_0^\star$ in terms of the free tropospheric $h^\star$ and the

solar forcing:

$$h_0^\star = h^\star + \frac{\sigma T_e^4}{\rho_s C_k |V_s|}. \tag{6}$$

We will now examine what governs the time scale of relaxation to equilibrium if the surface temperature T_s and tropospheric saturation MSE $h^\star$ are infinitesimally perturbed. (Note that our perturbations to $h^\star$ are taken to be constant with height, i.e., we perturb which moist adiabat the temperature profile follows. Non-constant perturbations would be adjusted to constancy on the fast convective timescale). We assume in our calculation that T_e, p_e and V_s remain constant. The linear dynamical equations for the evolution of the saturation MSE perturbation $h^{\star\prime}$ and surface temperature perturbation T_s' are then

$$\frac{\Delta p}{g} \frac{\mathrm{d}h^{\star\prime}}{\mathrm{d}t} = -\frac{\partial F_\mathrm{rad}}{\partial h^\star} h^{\star\prime} + F_c' \tag{7}$$

$$c_\ell \rho_\ell \Delta z_\mathrm{ML} \frac{\mathrm{d}T_s'}{\mathrm{d}t} = -F_c'. \tag{8}$$

Here Δp is the pressure thickness of the troposphere, $\Delta p = p_\mathrm{surface} - p_\mathrm{tropopause}$, ρ_ℓ is the density of liquid water, c_ℓ is the heat capacity of liquid water, Δz_ML is the mixed layer depth, and F_rad is the net upwelling IR radiation at the top of the atmosphere. In equation (7), the $\Delta p/g$ factor results from integrating the density of air through the troposphere to calculate the tropospheric heat capacity using hydrostatic balance. Equation (7) is the linearization of the tropospheric MSE balance, while equation (8) is the linearization of the surface energy balance.

In their current form the linear evolution equations are not closed as we do not know $\partial F_\mathrm{rad}/\partial h^\star$ or F_c'. Using the chain rule, the relationship (6) between $h^\star$ and $h_0^\star$, and the Clausius-Clapeyron relation we write

$$\frac{\partial F_\mathrm{rad}}{\partial h^\star} = \frac{\partial F_\mathrm{rad}}{\partial T_s} \frac{\partial T_s}{\partial h^\star} = \frac{B}{1 + \frac{L_v^2 q_s^\star}{c_p R_v T_s^2}}, \tag{9}$$

in which we have defined $B \equiv \partial F_\mathrm{rad}/\partial T_s$ to be the climate sensitivity parameter. Here R_v is the water vapor gas constant, and subscript s indicates surface values so that $q_s^\star$ is the surface saturation specific humidity. Note that T_s refers to the basic state value of the surface temperature and not its linear deviation. The quantity B depends on the structure of GHGs and other factors, but is for simplicity here treated as a constant, taken from the single column model. The linear variation of the convective flux F_c' is given by

$$F_c' = \rho_s C_k |\mathbf{V}_s| \left(h_0^{\star\prime} - h^{\star\prime} \right) \tag{10}$$

which completes the closure of (7,8).

To cast our simple model into its final form, we re-write our surface temperature perturbation T_s' in terms of the perturbation to the surface saturation MSE $h_0^{\star\prime}$ using the relation

$$T_s' = \frac{h_0^{\star\prime}/c_p}{1 + \frac{L_v^2 q_s^\star}{R_v c_p T_s^2}} \tag{11}$$

68

and nondimensionalize according to the following definitions:

$$A \equiv \rho_s C_k |V_s| c_p \qquad b \equiv 1 + \frac{L_v^2 q_s^\star}{R_v c_p T_s^2} \qquad \chi \equiv \frac{Ab}{B + Ab} \tag{12}$$

$$\tau_a \equiv \frac{c_p \Delta p b}{g(B + Ab)} \qquad \tau_o \equiv \frac{c_\ell \rho_\ell \Delta z_{\mathrm{ML}}}{Ab}. \tag{13}$$

After these manipulations we arrive at the final form of our analytical linear model:

$$\tau_a \frac{\mathrm{d} h^{\star\prime}}{\mathrm{d} t} = -h^{\star\prime} + \chi h_0^{\star\prime} \tag{14}$$

$$\tau_o \frac{\mathrm{d} h_0^{\star\prime}}{\mathrm{d} t} = h^{\star\prime} - h_0^{\star\prime}. \tag{15}$$

In these equations, τ_a is an atmospheric relaxation timescale and τ_o is an ocean surface timescale. The nondimensional parameter χ plays an important role in the linear dynamics and has value $\chi \sim 0.9$ for our current climate. We now use this two-dimensional linear system of ordinary differential equations to examine how ocean-atmosphere coupling affects the timescale of return to RCE.

Consider first the artificially restricted case in which the ocean surface temperature is held fixed, so that $T_s' = 0$ (and correspondingly $h_s' = 0$). The atmospheric temperature profile then returns to its original moist adiabat on the atmospheric timescale τ_a, which for our current climate has the value $\tau_a \sim 10$ days. In the correspondingly restricted case for the ocean in which the ocean surface temperature is perturbed holding the atmosphere fixed, the ocean surface returns to its equilibrium temperature on the ocean timescale $\tau_o \sim 100$ days.

We now consider the general solution for the decay timescale of perturbations away from RCE by computing the eigenvalues of the 2×2 matrix characterizing our linear dynamics. We find that the least damped eigenmode decays according to the timescale

$$\tau = \frac{2\tau_o}{1 + \frac{\tau_o}{\tau_a} - \sqrt{\left(1 + \frac{\tau_o}{\tau_a}\right)^2 - 4(1 - \chi)\frac{\tau_o}{\tau_a}}}. \tag{16}$$

It is informative to investigate the behaviour of τ in two interesting limits: $\tau_o \gg \tau_a$, and $\tau_o \ll \tau_a$. In the case in which the oceanic timescale is much longer than the atmospheric timescale, we find that

$$\tau \sim \tau_a + \frac{\tau_o}{1 - \chi}. \tag{17}$$

This timescale is longer than either the atmospheric or oceanic timescales, and can be very large if χ is close to 1. In the case in which the atmospheric timescale is much longer than the ocean timescale, we obtain

$$\tau \sim \frac{\tau_a}{1 - \chi} \tag{18}$$

which is also larger than either τ_a or τ_o (as $\tau_a \gg \tau_o$), and can also grow large if χ is close to 1. This analysis indicates that the timescale for return to equilibrium for a coupled system is always longer than the atmospheric timescale. Even in the limit of a very thin mixed

69

layer ($\Delta z_{\mathrm{ML}} \to 0$), in which case τ_o becomes very small, the timescale for the return to equilibrium can still be much longer than the atmospheric timescale τ_a as a result of the factor $(1 - \chi)$ appearing in the denominator due to the atmosphere–ocean coupling. This effect can be seen in general circulation models, which require much longer integrations to reach equilibrium when coupled to an ocean.

The linear model defined by equations (7) and (8) performs well when compared to a single-column model in spite of its apparent simplicity. Figure 8 shows a comparison of the return rate to equilibrium as calculated from the analytical model alongside best fit decay rates measured in a single-column model. The single-column model was used to measure the climate sensitivity parameter B which appears in the linearized dynamics. The degree of agreement between the simple model and column model is impressive both in the approximate numerical magnitude of the timescale as well as in the dependence of the timescale on the mixed layer and the surface temperature of the equilibrium state.

Theory　　　　　　　Single-column Model
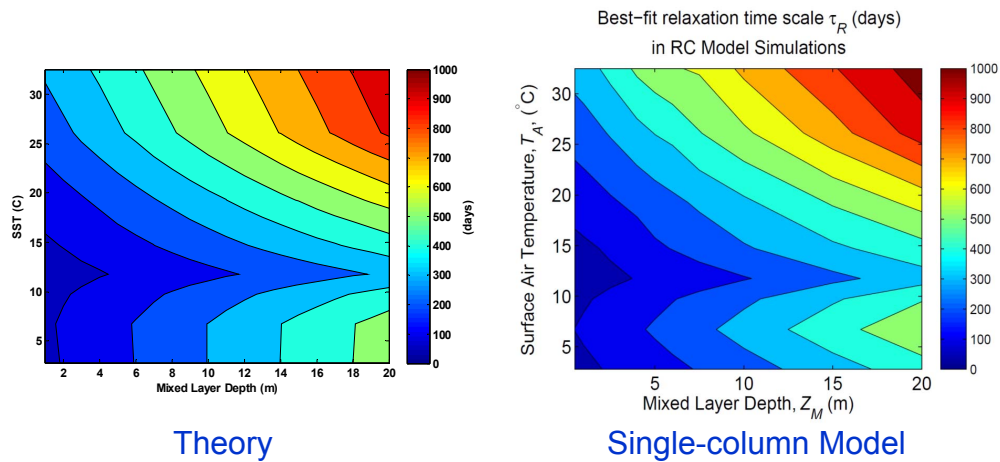
Figure 8: Comparison of the return timescale to RCE between the analytical linear model and a single-column model. The single-column model is used to parameterize the analytical model through the single climate sensitivity parameter B. The agreement between the simple theory and the numerical model is apparent.

5　Explicit Simulation of Radiative-Convective Equilibrium

We next turn our attention to a problem at the frontier of research in atmospheric science: convective aggregation. The numerical modeling and analysis in this section follows a recently published paper: Wing, A. A., and K. A. Emanuel (2014), Physical mechanisms controlling self-aggregation of convection in idealized numerical modeling simulations, *J. Adv. Model. Earth. Syst., 6, 59-74*, doi:10.1002/2013MS000269.

5.1　Model Observations of Convective Aggregation

The study of convective aggregation requires a more sophisticated modelling approach than we have taken so far in these lectures. We now move from simple dynamical systems models

and single-column models to idealized three-dimensional simulations of moist convection using the cloud-resolving model SAM (System for Atmospheric Modelling). The model geometry and forcing are shown in Fig. 9. The domain is doubly periodic in the horizontal with rigid boundaries at the top and bottom. The model is forced by fixed and spatially homogeneous sea surface temperatures (SSTs) in the range of 297–312 K at the lower boundary and a constant value of the solar forcing set to be 413.98 W/m^2. The domain size is 768 km $\times$ 768 km $\times$ 28 km, with a horizontal resolution of 3 km and 64 levels in the vertical. The initial conditions are specified according to a profile computed from the domain average of a previous model run of radiative–convective equilibrium in a smaller domain. The model resolution permits the marginal resolution of moist convection, and the model features a fully-interactive rapid radiative transfer model (RRTM), cloud microphysics, as well as surface fluxes.
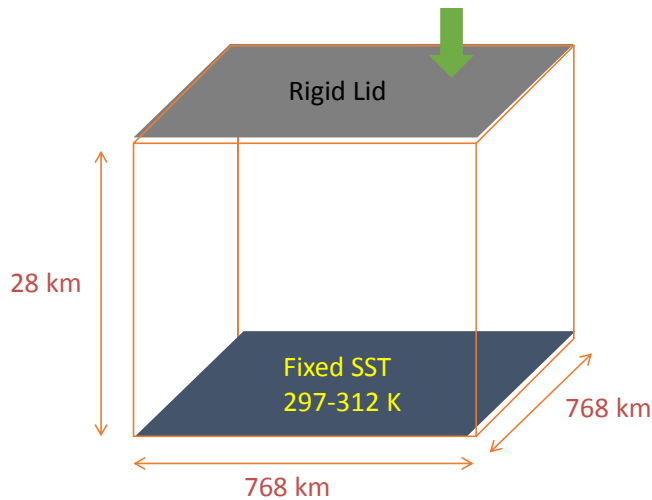
Figure 9: Schematic of the domain used in cloud-resolving modelling to study convective aggregation.

When the cloud-resolving model is run in this configuration for a sufficiently long time, the convection, which is initially statistically homogeneous and apparently random, spontaneously focuses into a cluster. This can be visualized in two dimensions by plotting the vertically-integrated water vapor (also referred to as the total precipitable water, or TPW) at various times throughout the model integration. Figure 10 (left) shows the time-averaged TPW over the first day of model integration as a function of (x, y) for a case in which the SST is set at 305K. The moisture field at each point in space is near its spatial average value. As the integration continues, TPW becomes spatially inhomogeneous. Figure 10 (right) shows the average TPW on Day 10. A relatively dry area is seen to form in the upper left corner of the domain. The temporal and spatial evolution of this dry patch, or "hole", can be seen in Figs. 11–14. By Day 90, the hole has expanded to cover most of the outer edge of the (periodic) domain, and the convective region (the complement of the hole) has become focused at the centre of the domain. We note that the boundary conditions and forcing for this problem are spatially homogeneous, so that the final position of the convecting region (the red region in Fig. 14) is random and dependent on the structure of

the noise in the initial conditions. We also note that the spatial structure of the convective cluster/hole system has a complex time evolution, sometimes forming horizontal bands as can be seen in Fig. 13. This phenomenon of hole formation followed by convective clustering is often referred to under the name "convective aggregation" and has been observed in a variety of cloud-resolving models. However, the evolution shown in Figs. 10–14 indicates that the convective cluster actually results from the initial formation of a small hole in the otherwise statistically homogeneous convection, and so perhaps the phenomenon could be more accurately called "convective self-annihilation".
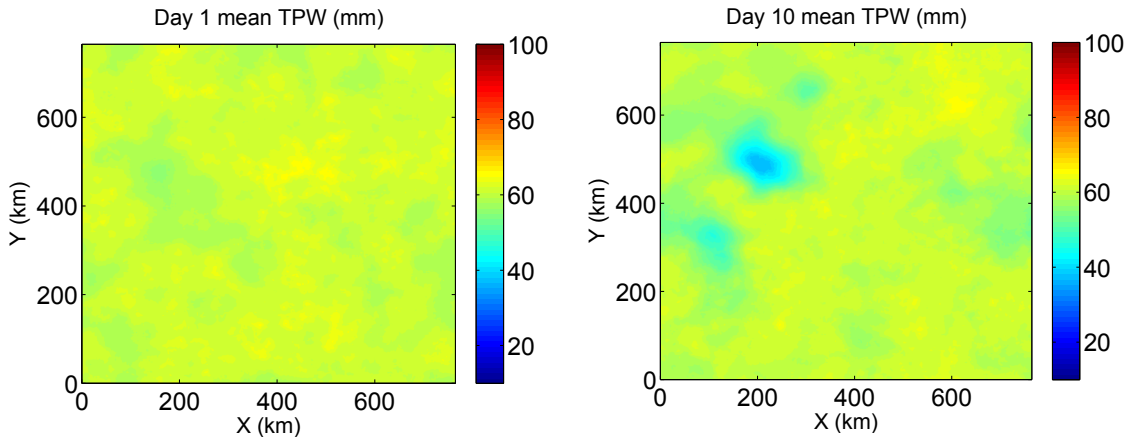
Figure 10: Average total precipitable water (TPW) over Day 1 (left) and Day 10 (right) during a cloud-resolving model simulation in the configuration shown in Fig. 9. The SST is set at 305K. Note the formation of a small hole in the convection on Day 10 in the upper left corner of the domain.
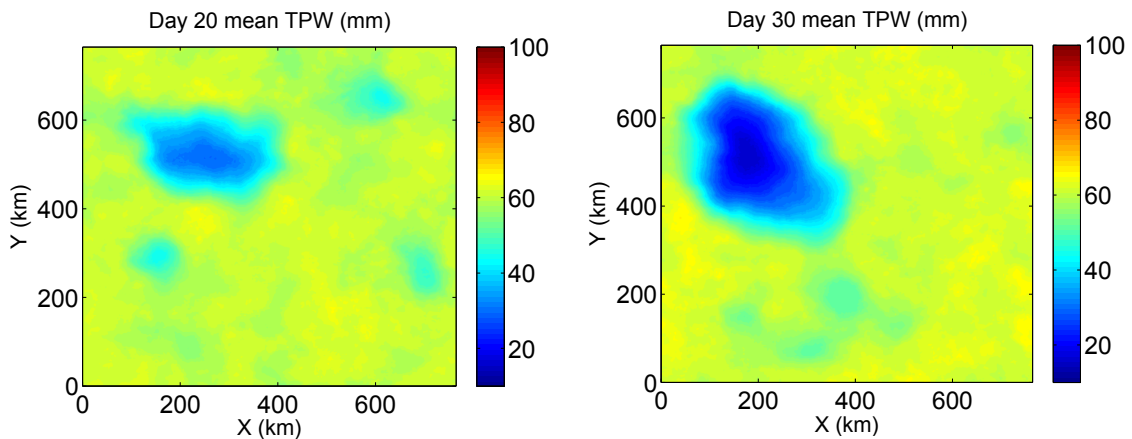
Figure 11: As in Fig. 10, but for Day 20 (left) and Day 30 (right).

Two physically interesting and important questions concerning convective aggregation are: 1) What controls the spatial scale of the final cluster? 2) How does convective ag-
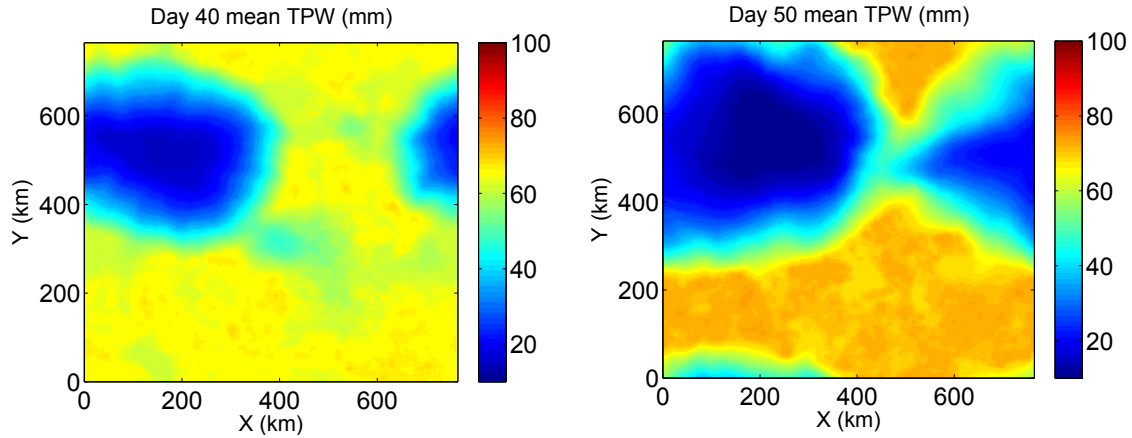
Figure 12: As in Fig. 10, but for Day 40 (left) and Day 50 (right).
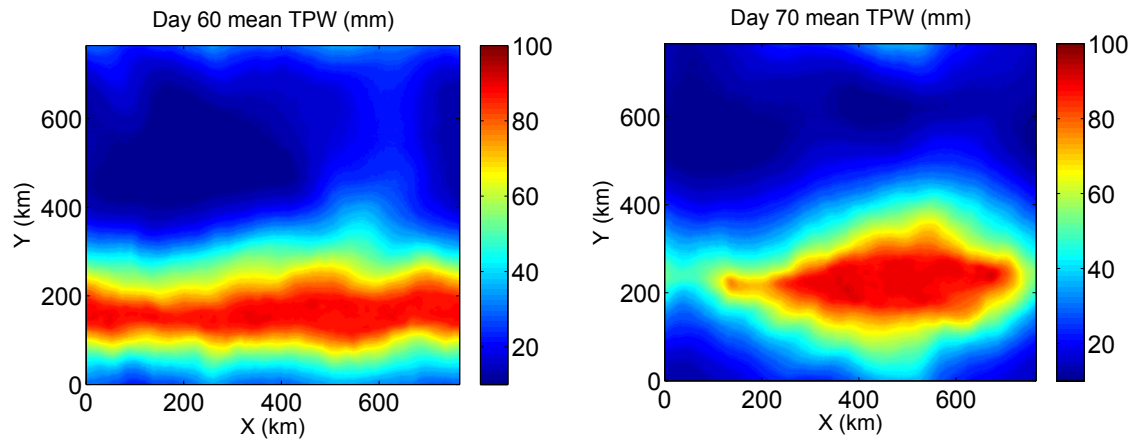
Figure 13: As in Fig. 10, but for Day 60 (left) and Day 70 (right).

gregation depend on the imposed SST? The answers to these questions are not completely understood. Toward addressing the first question, it is observed in nonrotating cloud-resolving model simulations that convective clustering always results in a final cluster state that takes on the scale of the domain. An example of this can be seen in Fig. 14, in which there is only one convectively active (bright red) region, with the rest of the domain being dry and quiescent. If simulations are run in a larger domain, the size of the final cluster increases as well. It has also been found that convective aggregation does not occur if the simulation is run in a sufficiently small domain. We will discuss a physical hypothesis for explaining this observation in the next lecture. We note before proceeding that it is relevant to ask whether our fixing of SSTs results in an effective forcing of the convective cluster once it has formed. Such an effect could arise because we do not allow the SST to adjust under the convective region, thereby excluding the shadowing effect the clouds would have on the surface. It would be important to test the effect of variable SSTs on cluster formation by coupling our cloud-resolving model to a slab ocean. However, such computations are very
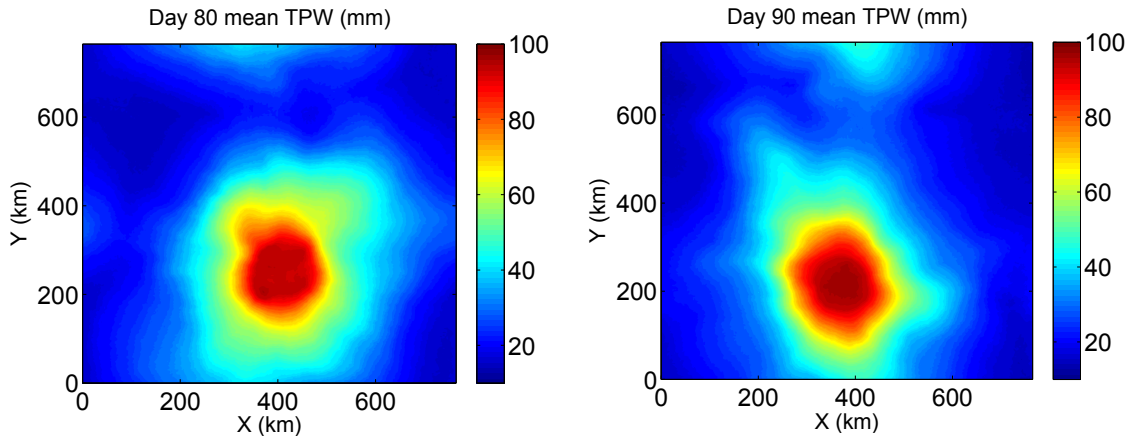
Figure 14: As in Fig. 10, but for Day 80 (left) and Day 90 (right).

expensive to run to equilibrium as the time scale for equilibration becomes very long due to the coupling, as discussed previously in this lecture. It is not currently known whether convective aggregation occurs when coupled to an interactive ocean surface.

To address the dependence of convective aggregation on SST, we examine the results of our cloud-resolving model simulations for different fixed, spatially-constant SST values. Figure 15 shows the time evolution of the outgoing LW radiation (OLR) for a variety of simulations with different SSTs. After an initial transient equilibration period, all integrations reach an approximate statistical equilibrium after a few days with OLR in the range of 250–270 W/m^2. After this period, some model runs show a significant increase in OLR, indicating that this initial statistical equilibrium is unstable. This increase in OLR is a signal that convective aggregation is occurring: LW flux to space increases when the convection aggregates as there is very little water vapor outside the cluster, and the cluster occupies a relatively small areal fraction of the domain. The SST values for each integration are shown in the panel on the RHS of Fig. 15. Inspection of the SST values reveals an apparent transition point in the large-scale behaviour of the convection as a function of SST. For the relatively low SST values 297 K, 298 K, 300 K (dark blue and black lines with OLR ~ 255 W/m^2 after the transient), the OLR appears to remain statistically steady, and the convection remains statistically homogeneous. As the SST is increased beyond 300 K, the behaviour transitions to convective organization: model integrations for 301–307 K show increasing OLR associated with convective aggregation beginning around 40 days. These results suggest that 300 K is an SST threshold above which convection aggregates and below which convection remains statistically homogeneous. We note that the time required for the clustering to complete appears to depend on the initial noise in the system and varies between model runs, although the *rate* of increase of OLR appears to be determined by the boundary conditions and forcing.

A complication appears to arise as we continue to increase SST above 307 K. The integrations for 310 K, 311 K, and 312 K, shown in purple/red/dark orange, appear to have constant OLR ~ 275 W/m^2, never forming a convective cluster. This appears to indicate a non-monotonic dependence of convective clustering on SST. However, this behaviour may

74

be artificial. An additional model run with an SST value of 310 K but with the size of the domain doubled is shown by the red curve that exhibits increasing OLR and that has the highest final value of OLR at day 100. Although the 310 K run with the standard domain size does not aggregate, a cluster does form in the enlarged domain. This suggests that the apparent lack of monotonicity may actually indicate that the critical domain size beyond which clustering is possible depends on temperature: we may need to use systematically larger model domains to observe clustering as we increase SSTs. As the calculations are expensive, however, it is not currently feasible to continually increase the domain size and test whether all higher SST cases aggregate given a sufficiently large domain.

This leaves us with the impression that the critical temperature above which aggregation happens is about 300 K or 27°C. This is suspiciously close to the tropical surface temperature in the current climate. This may be a coincidence, but we will speculate that it arises from a self-regulatory process in the next lecture.

Aggregation similarly happens in climate models, affecting dramatically the simulated climate. Whether clusters in these models form for the right reasons is an open question. Clusters are, of course, also observed in the real world, giving us confidence that aggregation plays an important role in the present climate.
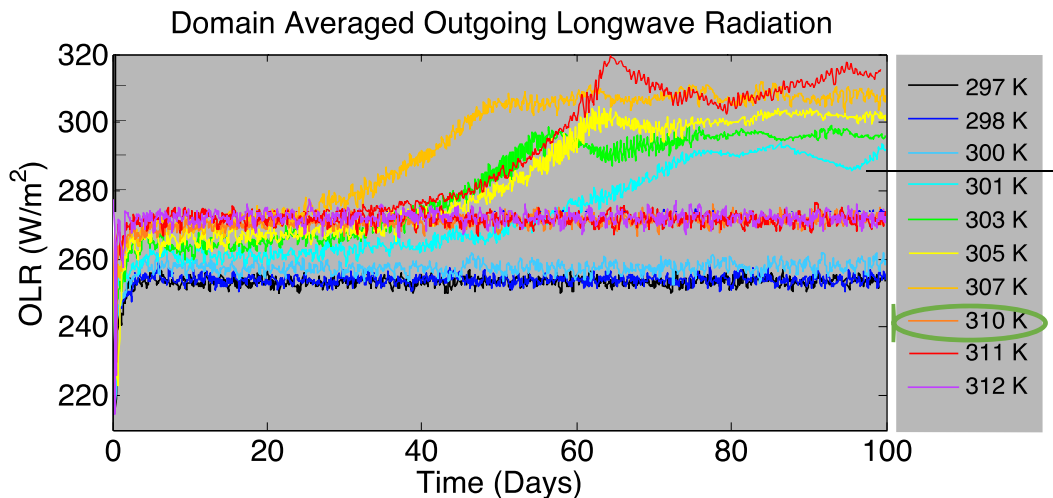
Figure 15: Time evolution of the outgoing longwave radiation (OLR) for various cloud-resolving model runs with different fixed SSTs (right). Increases in OLR after the initial equilibration period indicate the formation of a convective cluster.

5.2 Energy Budget during Aggregation

To better understand the feedback processes involved in convective aggregation, we now examine the energy budget throughout the domain and as a function of time. We will work with the mass-weighted column integral of the frozen moist static energy (FMSE), defined as

$$h = c_p T + gz + L_v q_v - L_f q_i \tag{19}$$

75

in which we now use the symbol q_v to indicate the water vapor mixing ratio, q_i is the ice mixing ratio, and L_f is the latent heat of fusion of water. We will denote the mass-weighted vertical integral operator using a caret: $\hat{h}$. The vertically integrated FMSE $\hat{h}$ is not changed by moist convection, which is a transport process, but can be only be changed by radiation, surface fluxes, and horizontal transport. We will consider the deviations of $\hat{h}$ from the horizontal mean, and denote these deviations by $\hat{h}'$. The evolution equation for $\hat{h}'$ is

$$\frac{\partial \hat{h}'}{\partial t} = \mathrm{LHF}' + \mathrm{SHF}' + \mathrm{NetSW}' + \mathrm{NetLW}' - \boldsymbol{\nabla}_h \cdot \widehat{\mathbf{u}h} \tag{20}$$

where LHF is the surface latent heat flux, SHF is the surface sensible heat flux, NetSW is the column SW radiative flux convergence, NetLW is the column LW radiative flux convergence, and $\boldsymbol{\nabla}_h \cdot \widehat{\mathbf{u}h}$ is the advective transport term, with $\boldsymbol{\nabla}_h$ denoting the gradient operator in the horizontal. Note that the advection term has zero mean as it is a flux divergence. The evolution equation for the variance of $\hat{h}'$ is obtained by multiplying eq. (20) by $\hat{h}'$:

$$\frac{1}{2}\frac{\partial}{\partial t}(\hat{h}')^2 = \hat{h}'\mathrm{LHF}' + \hat{h}'\mathrm{SHF}' + \hat{h}'\mathrm{NetSW}' + \hat{h}'\mathrm{NetLW}' - \hat{h}'\boldsymbol{\nabla}_h \cdot \widehat{\mathbf{u}h}. \tag{21}$$

The variance of FMSE is a useful quantity to examine because it increases with the degree of convective aggregation. The source and sink terms in eq. (21) are correlations between the mass-weighted column-integrated FMSE and the various diabatic terms as well as with the horizontal convergence of $\hat{h}$. When one of these correlations is positive, that term contributes to self-aggregation by either drying a relatively dry region or moistening an already moist region. By examining the sign and magnitude of these RHS terms, we will be able to identify the effect that each of these physical processes has on the formation of convective clusters. In the analysis, the LHF, SHF, NetSW, and NetLW terms are calculated from the model. The horizontal convergence term is then diagnosed as a residual.

To visualize the results of the analysis, each RHS term is calculated and then averaged over each non-overlapping 48 km × 48 km subdomain and also averaged over one day. For each RHS term, the average values for each subdomain are then ordered according to the subdomain's average value of the column relative humidity, from dry to moist. This ordering procedure allows us to visualize the effect of each term in the FMSE variance budget as it depends on both time and moisture. We also normalize each term by the instantaneous horizontal mean value $\{(\hat{h}')^2\}$, where curly braces indicate the horizontal average. This normalization prevents the early stages of the dynamics from being washed out due to the smallness of the FMSE variance as well as the smallness of the individual RHS budget terms. Figure 16 shows an example of such a visualization from the 305 K run, whose OLR can be seen as a function of time in Fig. 15. In Fig. 16 the x-axis gives the columns ranked by their moisture content, while the y-axis shows time evolution from 0 to 90 days. Colors show the value of the correlation between $\hat{h}'$ and the total diabatic term, that is, the contribution to the rate of change of $(\hat{h}')^2$ from

$$\hat{h}'\mathrm{LHF}' + \hat{h}'\mathrm{SHF}' + \hat{h}'\mathrm{NetSW}' + \hat{h}'\mathrm{NetLW}'. \tag{22}$$

The black line running vertically through Fig. 16 is the $\hat{h}' = 0$ contour: the line separating the relatively dry columns from the relatively moist columns. We note that this way of

76

presenting the x-axis does not track the actual values of the column moisture. Over time, the range of column relative humidities from the driest to the moistest may increase, so that the x-axis would expand over time if we tracked the absolute values of humidity rather than using the ranking system presented here.

$$\hat{h}'SEF' + \hat{h}'NetLW' + \hat{h}'NetSW'$$
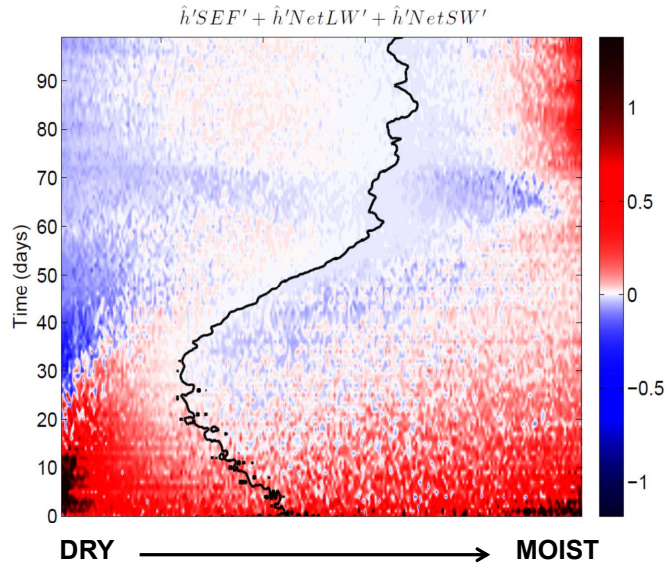
Figure 16: Contribution to the variance budget of mass-weighted column-integrated frozen moist static energy from the total diabatic term in the moisture-time plane. The x-axis orders air columns from driest to moistest, while time increases upward along the y-axis. Colors show the contribution to the variance tendency due to the sum of the diabatic terms on the RHS of eq. (21).

Figure 16 demonstrates that the total diabatic term on the RHS of eq. (21) acts to increase the FMSE variance in the first 20 days of the simulation, and that at early times the strongest correlations are observed in the dry regions. This is consistent with our observation that the convective clustering originates as a 'hole' seen to develop in the TPW field over time: increasing variance in dry regions corresponds to continued drying of the hole. These positive correlations then decrease in magnitude and shift into the moist regions, coinciding with the expansion of the hole into the convecting region.

Having examined the total effect of the diabatic terms on convective organization, we now consider them one at a time. Figure 17 visualizes the contribution to the rate of change of $(\hat{h}')^2$ from the column SW flux convergence NetSW. The SW flux convergence correlation is weak over most of domain for the majority of the integration with two important exceptions. Over the first 50 days in the driest regions, the SW effect is positive and tends to increase variance. This results from a feedback whereby dry columns ($\hat{h}' < 0$) absorb less solar radiation (NetSW$' < 0$) because water vapor is an important SW absorber. Negative solar absorption anomalies induce anomalous sinking, continuing to dry out the column. This positive feedback also acts in the moist regions once the convective cluster has formed. In the latter part of the integration (beyond 50 days or so) the moist regions have a strongly

positive SW effect because moist columns absorb more solar radiation leading to anomalous rising motion and moistening of the column. Both directions of this feedback act to enhance clustering and correspondingly increase the FMSE variance.

$$\hat{h}'NetSW'$$
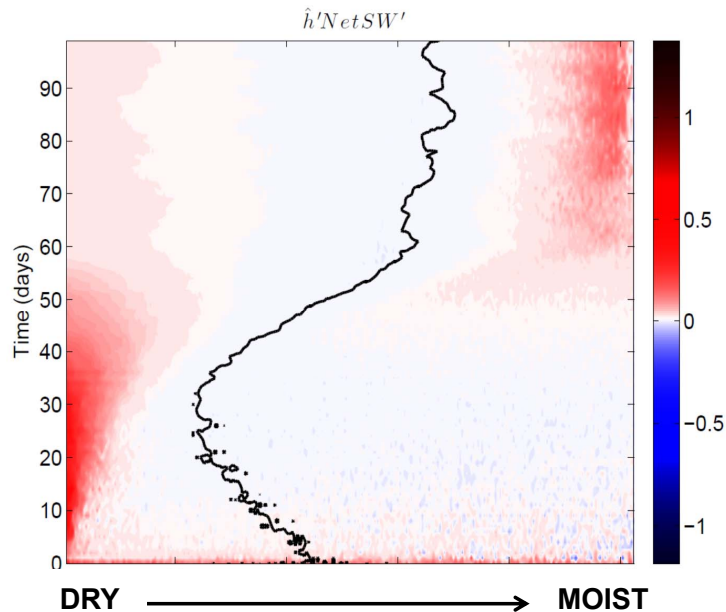
Figure 17: As in Fig. 16, but for the SW flux convergence.

The contribution to the FMSE variance from the LW term $\hat{h}'NetLW'$ is shown in Fig. 18. Early in the integration the LW contribution is essentially positive, but weakens after the first 20 days or so and is of varying sign in both relatively dry and relatively moist regions. However, once the convective cluster has been formed, the LW term is important for its maintenance. This can be seen in the top-right corner of Fig. 18, where the moistest columns (associated with the cluster) tend to have their FMSE variance increased by the LW effect. This feedback leads to hysteresis: once a cluster is formed, it is maintained by this effect, even if the SST is lowered below the critical value for the formation of clusters. The LW positive feedback is primarily due to the presence of high clouds that are opaque to LW radiation and have relatively low temperatures, reducing the LW emission to space. Anomalously low LW cooling manifests as a positive contribution in the anomaly energy budget $NetLW' > 0$, which has a positive correlation with $\hat{h}'$ in the moist columns within the convective cluster.

To discuss the effects of the surface fluxes LHF′ and SHF′ it is useful to decompose their fluctuations into components due to fluctuating winds and fluctuations in the air-sea disequilibrium in temperature and water vapor. We can write the surface enthalpy fluxes in terms of bulk formulae as

$$\text{LHF} = \rho c_E L_v U (q^{\star}_{Ts} - q_v) \tag{23}$$
$$\text{SHF} = \rho c_H c_p U (T_s - T_a) \tag{24}$$

where c_E is the latent heat exchange coefficient, c_H is the sensible heat exchange coefficient,

$\hat{h}'NetLW'$

DRY ⟶ **MOIST**
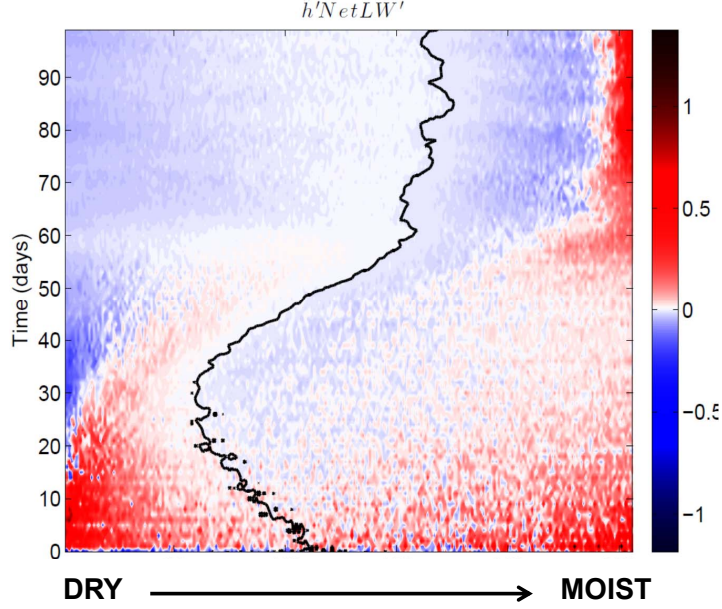
Figure 18: As in Fig. 16, but for the LW flux convergence.

U is the surface wind speed, T_s is the surface temperature, $q^{\star}_{Ts}$ is the saturation specific humidity at the surface, T_a is the atmospheric temperature at the lowest model level, and q_v is the specific humidity at the lowest model level. When computing the deviations from the horizontal mean of these enthalpy fluxes, we can isolate the total contribution from the fluctuations in surface wind speed:

$$\text{Surface flux wind feedback term} = \hat{h}'\rho L_v(c_E U)'\{\Delta q\} + \hat{h}'\rho c_p(c_H U)'\{\Delta T\}. \qquad (25)$$

Here the Δ symbol denotes the difference between the surface and the lowest model level as in eqns. (23) and (24). Figure 19 shows the effect of the wind fluctuation term in the moisture–time plane. This term is essentially positive everywhere and also contributes strongly to the maintenance of the cluster (upper right corner). This effect arises due to a positive feedback. The formation of the convective cluster produces more thunderstorms leading to anomalously strong surface winds. These enhanced surface winds produce greater surface enthalpy fluxes, so that the wind contribution to SHF + LHF is positive, giving a positive correlation with $\hat{h}'$ in the moist columns.

We now separately consider the contribution to the FMSE variance budget of the surface enthalpy flux anomalies due to fluctuations in the air–sea disequilibrium. From the bulk formulae (23) and (24) we obtain

$$\text{Surface flux air–sea disequilibrium feedback term} = \hat{h}'\rho L_v\{c_E U\}\Delta q' + \hat{h}'\rho c_p\{c_H U\}\Delta T'. \qquad (26)$$

Figure 20 shows the effect of this feedback term. The air–sea disequilibrium fluctuations act to reduce the tendency toward cluster formation everywhere in the domain and over all time periods. In the cluster region in particular, this surface flux acts to reduce the FMSE variance and weaken the cluster. This is due to a feedback. The presence of the convective

79

$$\hat{h}'\rho L_v(c_E U)'\{\Delta q\} + \hat{h}'\rho c_p (c_H U)'\{\Delta T\}$$

DRY ⟶ **MOIST**
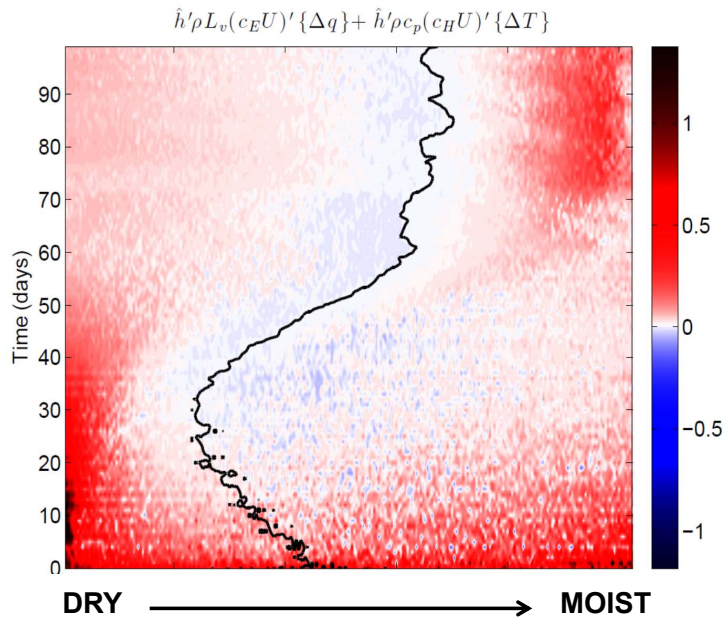
Figure 19: As in Fig. 16, but for the contribution to the total surface enthalpy flux from wind fluctuations.

cluster leads to moistening in the boundary layer. As a result, for a fixed surface wind speed, the boundary layer air has a specific humidity anomalously close to that of the ocean surface, leading to a negative anomalous surface enthalpy flux in a relatively moist region. This is a negative correlation and acts as a variance sink in the FMSE budget.

The combined effect of the surface flux feedback term is shown in Fig. 21. This includes the contributions discussed above due to U' and $(\Delta q', \Delta T')$ as well as additional contributions from $U'\Delta q'$ and $U'\Delta T'$. Comparison of the combined surface flux contribution with its components shown in Figs. 19 and 20 demonstrates that there is a large amount of cancellation in the FMSE variance budget between the mostly-positive effect of the wind fluctuations and the mostly-negative effect of the air–sea disequilibrium fluctuations. However, these cancellations are not complete. The net effect of the surface flux feedback is positive everywhere during the first 20 days of the integration, and is strongest in the dryest regions. The variations in strength and sign of this combined feedback term in the moisture–time plane demonstrate the effects of competing feedbacks controlling the development of the convective cluster.

For completeness, we show in Fig. 22 the contribution to the FMSE variance budget from horizontal divergence. This term is calculated as a residual from the rest of the budget, and is noisy and of varying sign in moisture–time space. This term can be computed more accurately by evaluating it directly, but the necessary quantities were not saved in the model simulation.

In the final lecture, we will try to understand the physics of aggregation. We will add rotation to our idealized model problem, taking us toward the dynamics of hurricanes and tropical cylones. The addition of rotation to the problem will provide an external scale for
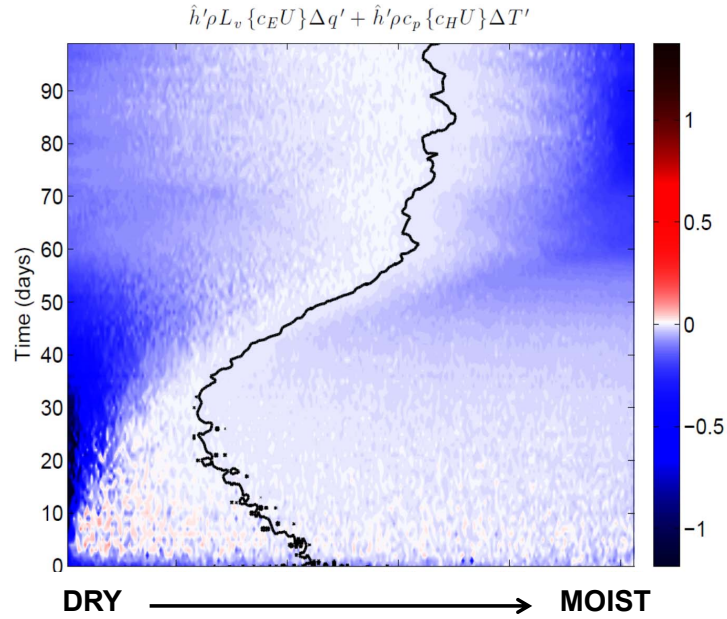
Figure 20: As in Fig. 16, but for the contribution to the total surface enthalpy flux from fluctuations in the air-sea thermodynamic disequilibrium.
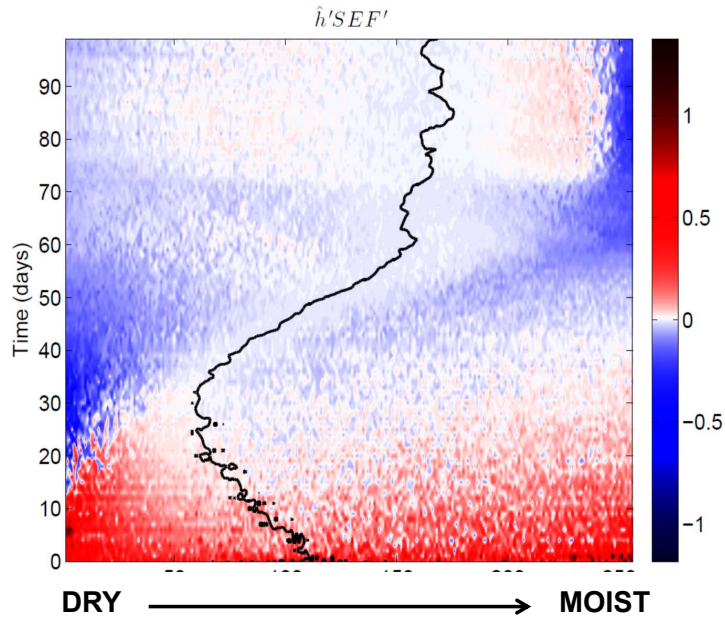
Figure 21: As in Fig. 16, but for the total surface enthalpy flux.

the problem, leading to scale-selection in the convective aggregation process. Using a linear stability analysis of the radiative–convective equilibrium, we will find that the physics when the hole is forming are different from the physics that sustain the cluster. The linear stability

81

$$\hat{h}\nabla \cdot \hat{uh}$$
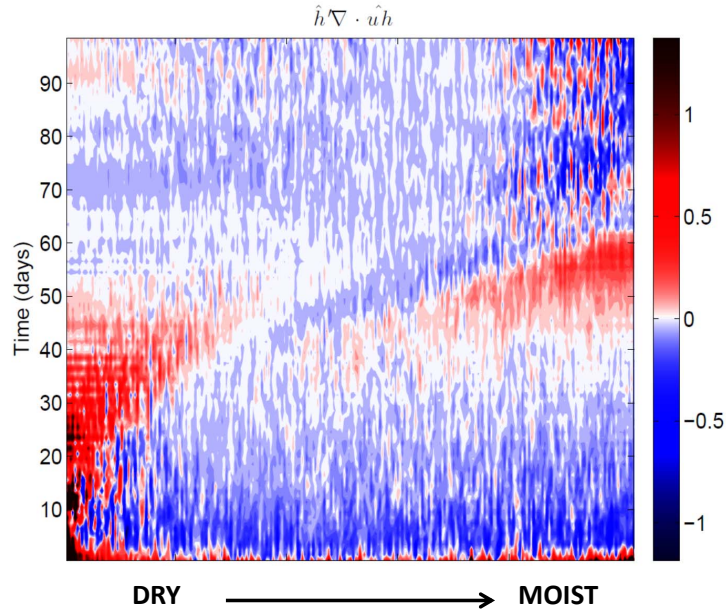
Figure 22: As in Fig. 16, but for the horizontal convergence. Note that this term is computed as a residual from the rest of the FMSE budget.

analysis will reveal that the initial instability depends on the temperature dependence of LW emissivity and help explain why aggregation only occurs at sufficiently large SSTs. In our analysis, we will make the weak temperature gradient approximation—in contrast to classic GFD problems, we thus parameterize the dynamics and focus our attention on the interaction of water substances and radiation. We will end with a speculative discussion of what we can infer from these idealized simulations for the real climate.